energies

MDPI

Article

Assessment of a Cost-Effective Multi-Fidelity Conjugate Heat Transfer Approach for Metal Temperature Prediction of DLN Gas Turbine Combustor Liners

Gianmarco Lemmi [1], Stefano Gori [2], Giovanni Riccio [2] and Antonio Andreini [1,*]

[1] Department of Industrial Engineering, University of Florence, Via S. Marta, 3, 50139 Florence, Italy; gianmarco.lemmi@unifi.it
[2] Baker Hughes, Via F. Matteucci, 2, 50127 Florence, Italy; stefano.gori@bakerhughes.com (S.G.); giovanni.riccio@bakerhughes.com (G.R.)
* Correspondence: antonio.andreini@unifi.it

Abstract

Over the last decades, Computational Fluid Dynamics (CFD) has become a fundamental tool for the design of gas turbine combustors, partly making up for the costs and duration issues related to the experimental tests involving high-pressure reactive processes. Nevertheless, high-fidelity simulations of reactive flows remain computationally expensive, particularly for conjugate heat transfer (CHT) analyses aimed at predicting liner metal temperatures and characterising wall heat losses. This work investigates the robustness of a cost-effective numerical setup for CHT simulations, focusing on the prediction of cold-side thermal loads in industrial combustor liners under realistic operating conditions. The proposed approach is tested using both Reynolds-Averaged Navier–Stokes (RANS) and unsteady Stress-Blended Eddy Simulation (SBES) turbulence models for the combustor flame tube, coupled via a time desynchronisation strategy with transient heat conduction in the solid domain. Cold-side heat transfer is modelled using a 1D correlation-based tool, runtime coupled with the CHT simulation to account for cooling-induced thermal loads without explicitly resolving complex cooling passages. The methodology is applied to a single periodic sector of the NovaLT^{TM}16 annular combustor, developed by Baker Hughes and operating under high-pressure conditions with natural gas. Validation against experimental data demonstrates the methodology's ability to predict liner metal temperatures accurately, account for modifications in cooling geometries, and support design-phase evaluations efficiently. Overall, the proposed approach offers a robust trade-off between computational cost and predictive accuracy, making it suitable for practical engineering applications.

Keywords: CHT; RANS; SBES; loosely coupled; industrial lean-premixed burner; gas turbine

check for updates

Academic Editor: Jiaqiang E

Received: 29 August 2025
Revised: 5 September 2025
Accepted: 11 September 2025
Published: 13 September 2025

Citation: Lemmi, G.; Gori, S.; Riccio, G.; Andreini, A. Assessment of a Cost-Effective Multi-Fidelity Conjugate Heat Transfer Approach for Metal Temperature Prediction of DLN Gas Turbine Combustor Liners. *Energies* **2025**, *18*, 4877. https://doi.org/10.3390/en18184877

1. Introduction

The prediction of combustor liner metal temperatures is critical to the design, durability, and operational reliability of gas turbine engines. These temperatures directly affect material selection, structural integrity, and maintenance intervals, particularly under the increasingly severe thermal loads associated with modern high-efficiency cycles [1,2]. Rising turbine inlet temperatures (TITs) and overall pressure ratios (OPRs) have pushed combustor components to operate in extreme environments [3,4], necessitating the use of advanced cooling technologies such as ribbed-channel convection, impingement, and effusion systems [5–7]. Although these cooling strategies offer effective thermal protection, their detailed numerical representation—especially in early design phases—remains challenging [8]. The complex geometries and small-scale features involved require high spatial resolution, making high-fidelity simulations computationally expensive. These difficulties are amplified in conjugate heat transfer (CHT) simulations [9,10], which are essential for accurately capturing the thermal interactions between fluid and solid domains, including convective, conductive, and radiative heat transfer.

At the same time, accurate predictions of metal temperatures are vital to prevent degradation, thermal fatigue, and mechanical failure. A reliable assessment of wall heat losses is also necessary, as these affect flame stabilisation and the overall aerothermal behaviour of the combustor [11,12]. To meet these requirements within realistic design timeframes, robust and efficient modelling frameworks are needed. Loosely coupled CHT strategies offer a promising solution by decoupling thermal processes across domains and allowing each mechanism to be solved with time discretisations appropriate to its characteristic temporal scale [13,14]. This temporal desynchronisation improves computational efficiency while maintaining thermal prediction fidelity. Several such frameworks have been successfully developed and validated, particularly for aero-engine combustor applications [15–18].

Turbulence modelling is another critical factor influencing heat transfer accuracy. Key phenomena such as flame anchoring, convective cooling, and pollutant formation are strongly governed by turbulent transport [19]. While Reynolds-Averaged Navier–Stokes (RANS) models are computationally affordable, they often fail to resolve the transient, three-dimensional nature of turbulent structures. As a result, scale-resolving approaches, including Large Eddy Simulation (LES) and hybrid methods such as Detached Eddy Simulation (DES) [20] and Stress-Blended Eddy Simulation (SBES) [21], have gained traction [22]. These approaches provide more accurate representations of unsteady reactive flows but come at significantly higher computational cost, especially in multiphysics contexts like CHT. From here, it is clear that the adopted CHT methodology must balance conflicting requirements. On one side, accurately resolving the reactive flow field necessitates unsteady, scale-resolving CFD methods, which require loosely coupled strategies to manage the large differences in characteristic time scales between heat conduction and turbulent transport. On the other side, the complex cooling features commonly employed on the combustor liner's cold sides make fully-resolved simulations computationally expensive. Uncertainties in cooling geometry and operating conditions further limit the practicality of high-fidelity CFD for predicting cold-side heat transfer during the design phase.

In this work, a hybrid, multi-fidelity numerical strategy is proposed to address the limitations of conventional CHT simulations during early design. The method combines a loosely coupled CHT framework—leveraging ANSYS Fluent's Solid Time-Step (STS) feature [23,24]—with a correlation-based 1D model that accounts for thermal loads imposed by external cooling systems. This setup reduces computational cost by avoiding explicit resolution of cooling passages and minimising mesh size, while still capturing the essential thermal behaviour of complex configurations such as ribbed or impingement channels.

The proposed framework is applied to a single periodic sector of the NovaLT$^{\text{TM}}$16 annular combustor, developed by Baker Hughes and operating under high-pressure conditions with natural gas. Both steady-state RANS and unsteady SBES simulations are conducted to assess the robustness and performance of the methodology.

The following sections present the computational domain and outline the mathematical formulation of the 1D model used for runtime evaluation of cooling-induced thermal loads. A comprehensive analysis of the results from both steady and unsteady simulations under the selected operating conditions is also provided.

2. Test Case and Investigated Operating Conditions

The numerical investigations are conducted on a single (periodic) sector of the NovaLT™16 annular combustor, manufactured by Baker Hughes (Figure 1). The burner operates with standard air, pre-heated to temperatures ranging from 580 to 700 K based on the operating point, along with natural gas featuring high C2+ content. The NovaLT™16 combustor introduces fuel into the primary zone through multiple injectors embedded in a high-velocity airstream, promoting effective mixing between the fuel and oxidiser to support efficient combustion. Fuel injection is carried out at ambient temperature. During this study, two distinct operating conditions of the combustor are investigated:

1. Test Point A (TP A): a high-load operating condition at approximately 17 bar, characterised by a uniform fuel distribution across the injectors.
2. Test Point B (TP B): a low-load operating condition at about 7 bar, featuring an imbalanced fuel distribution among the injectors.

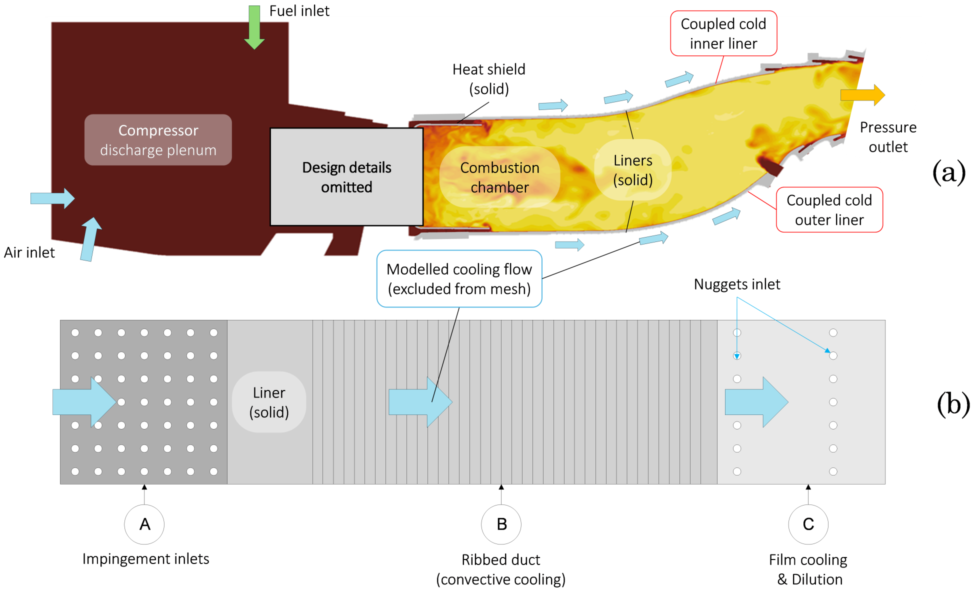

Figure 1. Computational domain: (**a**) single sector of the NovaLT™16 annular combustor; (**b**) schematic of liner walls. Burner design details omitted.

The cooling system is designed to regulate peak wall temperatures and safeguard components from degradation due to exposure to high-temperature gases within the chamber. Specifically, liner cooling is achieved through convection, utilising two ribbed channels (one inner and one outer), to promote turbulence and thereby enhance the external heat transfer coefficient (HTC). Conversely, an impingement system with multiple rows of cooling orifices is responsible for cooling the heat shield. Exhaust air from the ribbed channels is reintroduced into the combustion chamber through multiple rows of holes located at the nuggets. Along with the dilution holes, these contribute to shaping the temperature profile at the combustor outlet. Additionally, Thermal Barrier Coating (TBC), i.e., a thin layer of ceramic material with low thermal conductivity, is applied to the heat shield's internal surface and a portion of the liners' hot side.

3. Computational Domain and Numerical Setup

The geometry configuration encompasses both fluid and solid components, including the feeding plenum, the burner (including fuel supply lines), the combustion chamber, and the ribbed channels for liner cooling, constituting the fluid domain. Meanwhile, the solid domain comprises the liners and the metallic heat shield (HS).

Leveraging a correlation-based 1D model to compute the thermal loads associated with the external cold flow enables the exclusion of this portion of the cooling system from discretisation, thereby reducing the overall computational cost of the simulation. Further details of this modelling strategy are provided in Section 4.

All simulations are performed using the commercial pressure-based solver ANSYS Fluent® 2019 R1. The computational grid consists of a fully unstructured mesh comprising approximately 39 million polyhedral cells, with 5 million cells allocated for the solid domain. The grid features a general sizing of 2 mm, with local refinements applied to discretise regions of complex flow fields, ensuring accurate capture of the local mixing field. A 10-prism layer with a growth rate (GR) of 1.2 is generated for wall modelling, as illustrated in Figure 2.

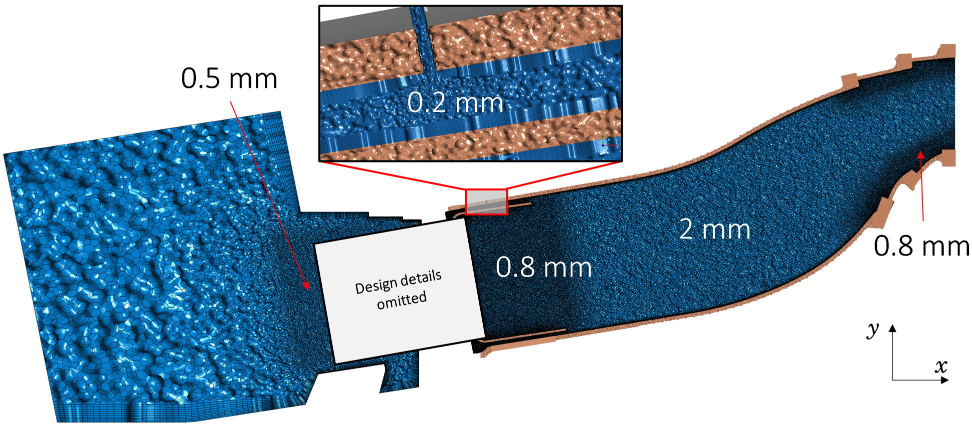

Figure 2. Computational grid on the $x - y$ plane of symmetry of the burner, showcasing enhanced mesh resolution in critical areas such as the primary zone, impingement jets, and dilution regions for detailed characterisation of the mixing process. Fluid and solid regions are colour-coded for clarity. Burner internals not shown for confidentiality.

Constant temperature and mass flow rate values of air and fuel are set at the respective inlet patches based on available experimental data for all simulations. At the combustor exit, a prescribed pressure outlet condition is applied, corresponding to the two different operating conditions investigated. Walls not included in the CHT simulation, namely those of the feeding plenum and burner, are treated as adiabatic. Each material assigned to these walls and to the solid domain is characterised by three key thermophysical properties: density, specific heat, and thermal conductivity. Material types are not disclosed due to confidentiality constraints.

As previously mentioned, the two simulated operating points (TP A and TP B), besides differing in load conditions, exhibit distinct distributions of fuel mass flow rates between the injectors.

3.1. Turbulence Modelling

As for turbulence modelling, a $k - \epsilon$ realisable model [25] with Enhanced Wall Treatment (EWT) [26] is used for the preliminary numerical campaign involving RANS simulations. For the subsequent scale-resolving simulations, an SBES (Stress-Blended Eddy Simulation) strategy is employed [21]. The SBES model is a hybrid RANS-LES turbulence approach that combines the robust formulation of the $k - \omega$ SST model [27] close to the walls—which means that wall stresses are computed through a RANS approach—and the ability of the LES model to resolve large structures in detached regions, i.e., subjected to massive separations and unguided flows. A shielding function developed within the SDES (Shielded Detached Eddy Simulation) framework [20] is extended to achieve a blending of the stress level between RANS and LES formulations [23]. In general terms, this affects the turbulence stress tensor in the following way:

$$\tau_{ij}^{SBES} = f_S \cdot \tau_{ij}^{RANS} + (1 - f_S)\tau_{ij}^{LES} \tag{1}$$

Here, τ_{ij}^{RANS} is the RANS portion and τ_{ij}^{LES} is the LES portion of the modelled stress tensor, with f_S indicating the shielding function. Further details on this turbulence-modelling approach can be found in the literature [23]. In this study, the Dynamic Smagorinsky–Lilly model [28] was used for sub-grid stress closure, in combination with a $k - \omega$ SST approach for solving near-wall regions, essential for accurately modelling turbulence within regions solved through a RANS approach.

Concerning numerical schemes, the Coupled algorithm [29] is utilised for pressure–velocity coupling in RANS simulations, with a Courant number set to 50. Spatial discretisation employs second-order accuracy across all equations. For the SBES simulations, the SIMPLEC algorithm (Semi-Implicit Method for Pressure-Linked Equations—Consistent) [30] is adopted for pressure–velocity coupling. Similar to the RANS setup, second-order spatial discretisation is applied, while time integration is handled using a Bounded Second-Order Implicit scheme, providing both accuracy and robustness for unsteady flow resolution.

Regarding the SBES campaign, the computational domain is initially simulated for a time equivalent to three flow-through times (FTTs) before activating the averaging procedure. To ensure statistically converged results, two additional FTTs are simulated.

3.2. Combustion Modelling

For turbulence combustion modelling, the Flamelet Generated Manifold (FGM) model is chosen for its computational efficiency while retaining the ability to accurately capture flame dynamics [31]. Within the FGM framework [32], thermodynamic quantities are parameterised using two control variables: the mixture fraction (Z), expressed according to Bilger's formulation [33], and the unnormalised progress variable, typically defined as $c = Y_{CO_2} + Y_{CO}$ for methane combustion. A 64 × 32 points look-up table in the $Z \times c$ control variables space is generated from the solution of diffusive flamelets using the GRI 3.0 detailed reaction mechanism, which encompasses 325 reactions and 53 species [34]. The turbulence–chemistry interaction is addressed through the use of a joint mass-weighted β-shaped Probability Density Function (PDF) of Z and c, requiring transport equations for both mean values ($\tilde{Z}$, $\tilde{c}$) and variances ($\widetilde{Z''^2}$, $\widetilde{c''^2}$) of the two control variables. In LES, however, the mixture fraction variance is modelled using an algebraic expression rather than a dedicated transport equation. The generic turbulent quantity ($\tilde{\phi}$) is then computed and stored in a look-up table, utilising the following expression:

$$\tilde{\phi}(Z,c) = \iint \phi(Z,c) P(Z,\tilde{Z},\widetilde{Z''^2}) P(c,\tilde{c},\widetilde{c''^2})\, dZ\, dc \tag{2}$$

Including the standard five governing equations, as well as the additional turbulence model transport equations (e.g., k and ε for RANS or k and ω for SBES) and the FGM transport equations, the total number of equations solved is 11 for RANS and 10 for LES. The Turbulent Flame Speed Closure (TFSC) by Zimont [35,36] is employed to model the mean progress variable source term, expressed as follows:

$$\bar{\dot{\omega}}_c = \rho_u S_t |\nabla \tilde{c}| \tag{3}$$

With ρ_u denoting the unburnt gas density. As per Zimont's model, the turbulent flame speed S_t is defined as

$$S_t = A u_{\Delta}'^{3/4} S_l^{1/2} \alpha^{-1/4} l_t^{1/4} \tag{4}$$

Here, u'_Δ is the modelled turbulent velocity fluctuations, l_t is the turbulence length scale, α is the thermal diffusivity of the unburnt gas, S_l is the unstrained laminar flame speed, and A denotes Zimont's model constant. In this study, A is set to 0.52 for RANS and 1.5 for SBES.

4. Conjugate Heat Transfer Modelling Approach

4.1. Cooling Flow: A Multi-Fidelity Approach

As previously indicated, the computational domain excluded the cooling ducts external to the combustion chamber to minimise computational costs. To account for the impact of the external cooling system, the heat flux extracted from the cold side of the liners is modelled by imposing HTC profiles and freestream temperature (T_{free}) along the axial coordinate of the machine. These profiles are dynamically computed using a 1D model coupled with the CFD solver, solving an energy balance radially for each liner segment, as schematically illustrated in Figure 3. The cooling channels are subdivided into numerous axial portions, where the outlet T_{free} of each portion is calculated based on an input T_{free} and an HTC obtained from correlation. Subsequently, this outlet T_{free} serves as the input T_{free} for the subsequent portion, enabling the calculation of convective heat flux extracted for each segment.

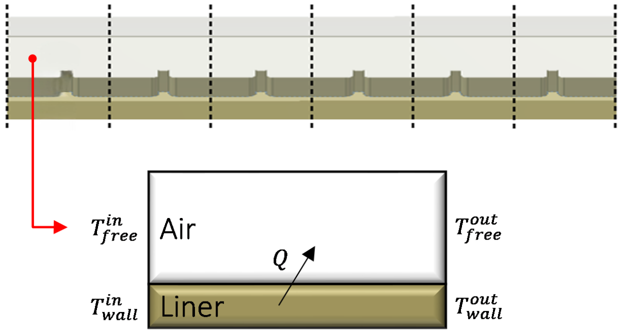

Figure 3. One-dimensional thermal exchange model for liners' cold side

The boundary conditions for the 1D model comprise the imposed inlet temperature and flow rate passing through the liner cooling passage, alongside parameters defining the cooling system's geometry, such as channel cross-sectional area and rib height. Correction coefficients are also applied to adapt the HTC correlation to the specific cooling system segment under analysis.

Specifically, the surfaces of the liners exposed to the external cold flow are divided into four main zones, as depicted in Figure 4, each treated with a different numerical approach for imposing the respective boundary conditions. Generally, non-adiabatic zones of the liners are treated with a convective heat flux condition imposed. The HTC and freestream temperature values are calculated at runtime using a correlation approach. These zone-specific conditions are updated iteratively every 10 iterations for RANS simulations and every 10 time-steps for scale-resolving simulations.

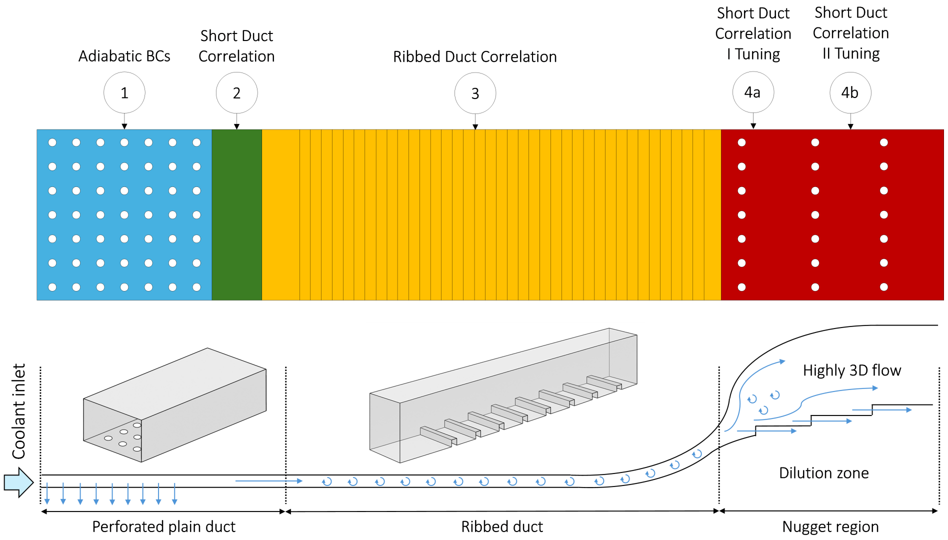

Figure 4. Heat flux modelling approach for the cold side of combustor liners (**top**) and schematic representation of the cooling system removed from the computational domain for clarity (**bottom**).

Delving deeper into the employed modelling approach, each main zone of the liners is modelled as follows:

1. The first zone, distinguished by the presence of impingement holes, is treated with an adiabatic boundary condition.
2. In the subsequent section, bridging the impingement zone and the onset of the ribbed channel, the heat transfer coefficient is determined using the Colburn–Kreith short ducts forced convection correlation for a fully developed turbulent flow:

$$Nu = 0.023\left(1 + 1.2\left(\frac{D_H}{l}\right)\right)Re^{0.8}Pr^{0.333} \tag{5}$$

$$HTC = \frac{\lambda}{D_H}Nu \tag{6}$$

   Here, Nu is the Nusselt number, D_H the hydraulic diameter, l is the characteristic length, λ the thermal conductivity of the fluid, Re the Reynolds number, Pr the Prandtl number, and HTC the convective heat transfer coefficient of the flow.

3. The convective heat transfer within the ribbed cooling channel is characterised using a proprietary correlation for the Nusselt number, developed internally by Baker Hughes. The formulation accounts for the primary geometrical and flow parameters influencing heat transfer performance in ribbed passages and is expressed in the general form

$$Nu = f\left(\frac{e}{D_H}, \frac{p}{e}, \frac{b}{w}, \theta, Re, \frac{T_2}{T_{\text{film}}}, Pr\right) \tag{7}$$

   Here, e, p, and w indicate the height, pitch, and width of the turbulator, respectively; b is the height of the duct, and θ is the rib angle to the mean flow direction. The air properties are evaluated at a mean temperature defined as

$$T_{film} = (T_1 + T_2)/2 \tag{8}$$

   with T_1 being the wall temperature and T_2 the total temperature of air relative to the surface.

The specific form of the correlation, including coefficients and exponents, cannot be disclosed due to its proprietary nature. However, it has been developed and validated based on an extensive review of existing correlations in the literature [37–40].

4. For the nugget zone, the HTC is calculated using the previously mentioned Colburn–Kreith correlation for short ducts. To provide a more accurate representation of the 3D flow conditions encountered by the portions of the liners, the nugget region is further partitioned into two distinct zones: one housing the first nugget (region 4a), and the other encompassing the second and third nuggets (region 4b). This segregation allows for the utilisation of distinct corrective coefficients for each zone, affording finer control over the HTC profile within the region and, consequently, enhancing the prediction of the cold-side liner metal temperature.

For modelling the Thermal Barrier Coating (TBC) positioned on the first part of the liners and the hot side of the heat shield, an equivalent thermal resistance is used, the latter computed based on the thickness and thermal conductivity of the material.

4.2. Loosely Coupled Conjugate Heat Transfer: Solid Time-Step

Concerning the loosely coupled CHT approach, the Solid Time-Step (STS) strategy integrated into the ANSYS Fluent solver is utilised. This method allows for time desynchronisation between the solid and fluid domains within the same simulation, enabling the use of different time-step sizes, coherently with their respective physical time scales, while maintaining consistent coupling at each global time increment. In this work, the fluid domain is advanced with a time-step of 1.5×10^{-5} s. while a significantly larger time-step of 1.5×10^{-2} s is employed for the solid domain, aligning with the characteristic timescales of conductive heat transfer. This strategy allowed the fluid domain to be simulated for a total duration of 70 ms and the solid domain for 70 s. Notably, this results in a considerable reduction in computational costs compared to strongly coupled (direct) CHT simulations, where both domains would necessitate simulation using the smallest time-step between them. Importantly, fluid–solid coupling is performed at every fluid time-step. This means that, although the fluid and solid domains advance using different time-step sizes, data exchange (in terms of instantaneous quantities such as temperature and heat flux) occurs at the frequency of the fluid solver (i.e., every 1.5×10^{-5} s in this case). The entire simulation is executed within a single Fluent session, adopting a concurrent parallelisation strategy where the fluid and solid solvers advance their respective time-steps simultaneously during the simulation, rather than solving one domain first and then the other in a sequential (or staggered) manner. A schematic representation of the STS loosely coupled approach is provided in Figure 5.

The STS methodology has been extensively validated by Amerini et al. [24], demonstrating its reliability and accuracy in aero-engine combustion applications. It thus represents a robust and scalable solution for high-fidelity CHT simulations in design and development contexts.

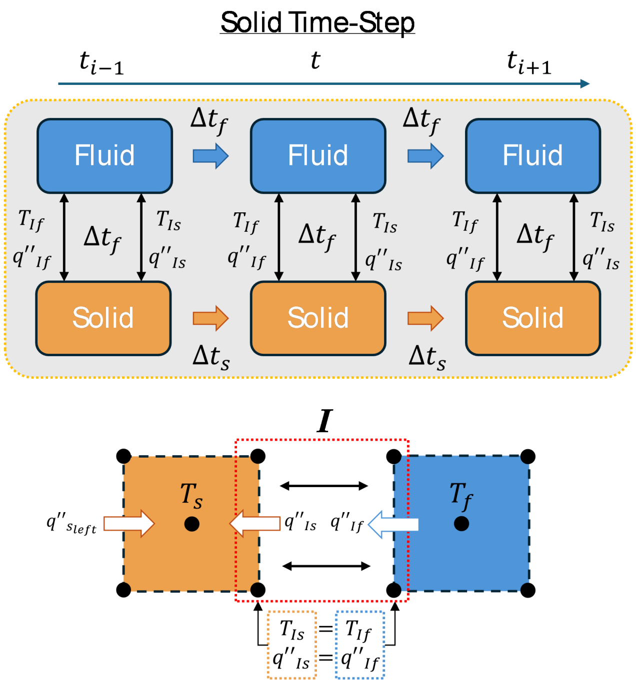

Figure 5. Schematic of the Solid Time-Step (STS) approach workflow.

5. Results and Discussion

In this section, the outcomes of the RANS and SBES simulation campaigns are presented. Initially, an evaluation of flow and temperature fields is provided to offer a comprehensive understanding of the combustion and flow dynamics within the burner. Subsequently, an assessment of the 1D model for computing the HTC profiles on the liners' cold side is conducted by comparing the predicted wall temperatures with experimental data from thermocouples.

Before delving into the aerothermal fields, an evaluation of the mesh quality is provided to demonstrate its suitability for capturing near-wall and turbulent flow structures. In particular, the y^+ distribution along the walls for both RANS and SBES simulations is presented in Figure 6. Overall, y^+ remains below 8, with local values ranging between 0.5 and 3 in the regions of greatest interest. This indicates that the first grid point lies within the viscous sublayer, allowing for accurate resolution of near-wall phenomena. It is worth noting, however, that in ANSYS Fluent, all turbulence models based on the ω-equation employ a y^+-insensitive formulation, ensuring consistency and robustness even at higher y^+ values [23,41].

In addition, the quality of the mesh for scale-resolving simulations is assessed through the shielding function and Pope Index, shown in Figure 7 for the SBES simulation. The shielding function contour, which assigns a value of 0 to the LES solution and 1 to the RANS solution, confirms the intended modelling strategy: the RANS approach, using the k–ω SST turbulence model, is applied only in the near-wall regions. Meanwhile, the Pope criterion assesses the fidelity of an LES (or SBES) simulation by evaluating the fraction of resolved turbulent kinetic energy relative to the total turbulent energy, expressed as

$$PI = \frac{k_{res}}{k_{res} + k_{sgs}} \tag{9}$$

where

- $k_{res} = 0.5(u^2_{RMSE} + v^2_{RMSE} + w^2_{RMSE})$
- $k_{sgs} = \frac{1}{0.3}\left(\frac{\nu_t}{C_s\Delta}\right)^2$

The Pope Index (PI) contour illustrates the quality of the SBES solution, revealing that the resolved fraction of turbulence in the combustion chamber exceeds 90%, indicating a high degree of fidelity in the simulation.

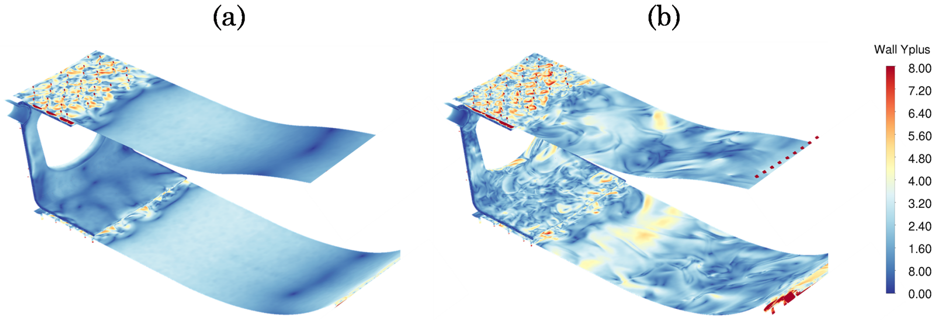

Figure 6. y^+ distribution along the walls for RANS (**a**) and SBES (**b**) simulations. No significant differences are observed in the near-wall resolution, apart from the expected smoother, averaged field in the RANS simulation compared to the more spatially resolved SBES counterpart.

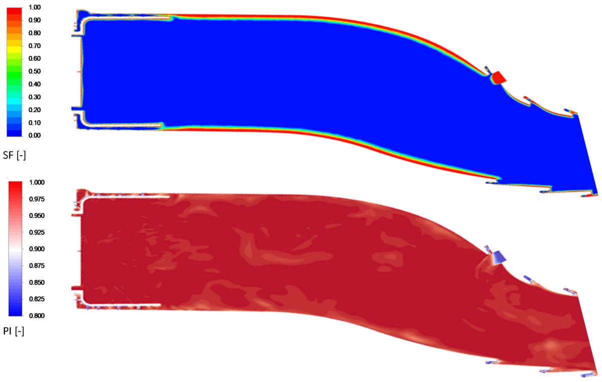

Figure 7. Time-averaged Shielding function (**top**) and Pope Index (**bottom**) contour maps on a longitudinal plane of the burner from TP A SBES simulation.

5.1. Test Point A

5.1.1. Aerothermal Fields

Figure 8 shows the time-averaged, normalised mixture fraction distribution on the domain midplane obtained from the SBES simulation. The results highlight the effectiveness of the mixing strategy, which facilitates rapid mixing of fuel and oxidiser immediately downstream of the dome. A nearly uniform mixture at the target equivalence ratio is achieved just beyond the heat shield and is maintained throughout the main combustion chamber, thereby ensuring combustion stability. Further downstream, the injection of external cooling air contributes to shaping the desired temperature profile at the inlet of the turbine's first stage. The mixture fraction field also reveals regions dominated by pure air introduced through the cooling system, specifically, the impingement jets on the heat shield and the dilution holes along the chamber wall. Notably, no substantial outer recirculation zone develops near the dome, favouring a downstream shift in the location of peak flame temperatures.

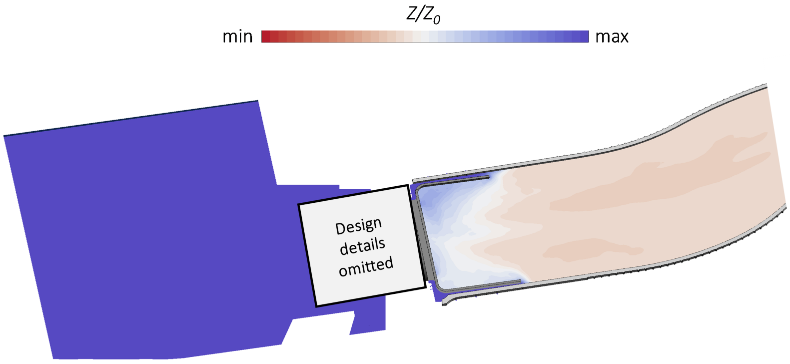

Figure 8. Normalised time-averaged mixture fraction field on a longitudinal midplane of the burner from the TP A SBES simulation. The solid domain is included to better illustrate the interaction between cooling flows and the combustor walls.

Figure 9 compares instantaneous and time-averaged contours of static temperature and axial velocity along the burner's plane of symmetry, derived from the unsteady SBES simulation and the steady RANS approach. The influence of the turbulence-modelling strategy is readily apparent. The RANS simulation predicts coherent and penetrating jet structures entering the chamber, with limited interaction between the high-momentum streams and the surrounding fluid. In contrast, the SBES results exhibit intensified shear-layer mixing, resulting in broader, more dispersed velocity and temperature fields and reduced gradient magnitudes. This enhanced turbulence shortens the axial reach of the high-velocity jets and alters both the shape and placement of the flame. The temperature field from SBES indicates that the high-temperature region extends closer to the liners, whereas in the RANS simulation, it remains confined to the central axis.

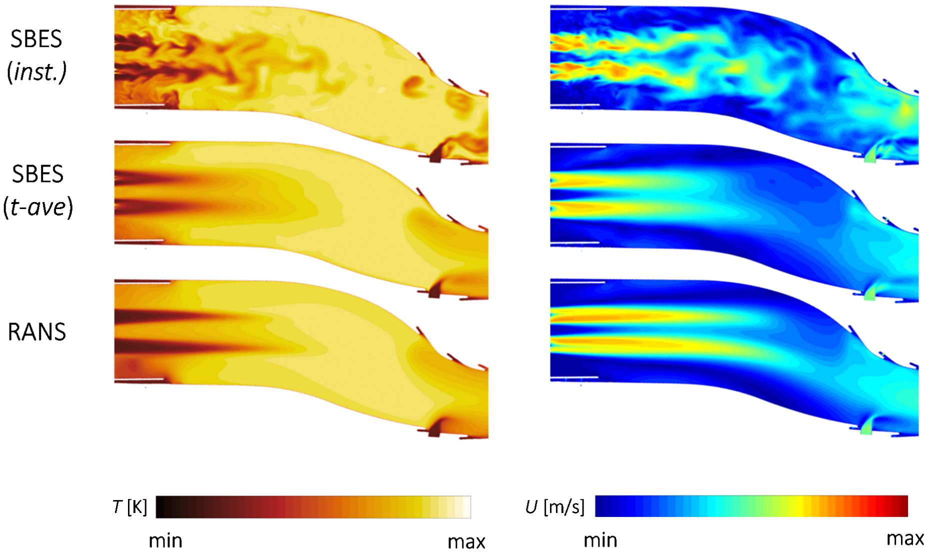

Figure 9. Normalised temperature and axial velocity fields on a longitudinal plane of the burner from TP A RANS and SBES simulations. The SBES results include both instantaneous and time-averaged data.

These distinctions are particularly relevant in the context of the present CHT analyses, as the differing flame shapes and jet penetration between RANS and SBES directly influence the distribution of thermal loads on the combustor walls. In particular, the broader and more dispersed flame predicted by SBES leads to greater thermal exposure of the liners, potentially affecting the accuracy of wall temperature predictions and, consequently, thermal management strategies in the design phase.

5.1.2. Liner Wall Temperature Distributions

The first part of the numerical campaign focused on validating the applicability of the coupled one-dimensional correlation-based approach integrated with 3D CFD simulations for predicting the convective heat transfer along the cooling air channels supplying the outer surfaces of the metallic liners. This preliminary activity represented a key milestone, as it allowed verification of the modelling strategy adopted for the cooling system and confirmed that the segmentation of the liners, as shown in Figure 4, is sufficient for properly capturing the convective heat transfer occurring within the cooling ducts.

Figure 10 presents the normalised wall temperature distribution along the axial direction of the cold-side centerlines of both inner and outer liners, along with the corresponding normalised heat transfer coefficients (HTCs, shown on the right-hand axis). The predicted temperature profiles between the impingement system and the ribbed section show good consistency with the thermocouple measurements acquired during the experimental campaign conducted by Baker Hughes. These results confirm that the numerical approach, despite relying on a one-dimensional treatment of the coolant side, provides a reliable estimate of the metal temperatures when coupled with high-fidelity CFD.

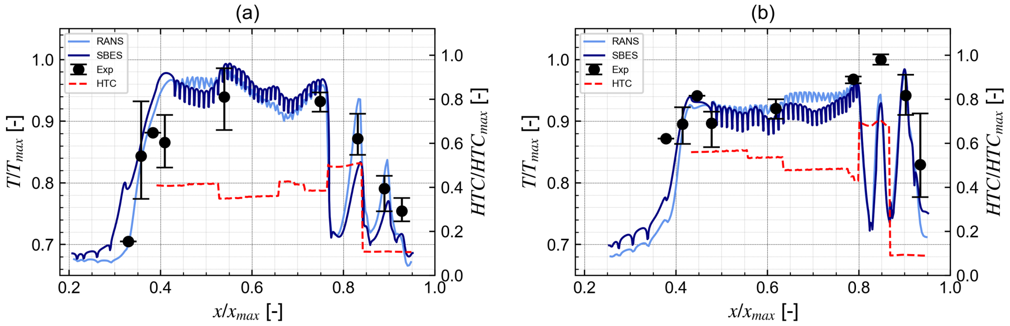

Figure 10. Normalised wall temperature and HTC distribution along the centerline of the cold-side walls for the inner liner (**a**) and outer liner (**b**).

Both the RANS and SBES simulations show satisfactory agreement with the experimental measurements, particularly in the ribbed region, where the flow conditions are relatively uniform and the correlation-based approach accurately captures the thermal gradient and wall temperature distribution. However, in the nugget region, the predictions diverge more significantly from the experimental data. This deviation is attributed to the highly three-dimensional and complex flow behaviour in this area, where large variations in cross-sectional area and interactions with dilution jets affect the local thermal field.

In the nugget region of the inner liner, the SBES simulation predicts lower wall temperatures than the RANS simulation for a given HTC. To match the same metal temperature, the RANS approach requires a significantly higher HTC (Figure 10), suggesting an overestimation of the thermal loads due to an inaccurate prediction of the jet dynamics and mixing behaviour near the cooling slots. SBES, by resolving more of the turbulent structures, captures the interaction between cooling and dilution jets more accurately (Figure 11). This results in enhanced mixing, reduced peak temperatures, and more realistic heat transfer rates, particularly in regions where coherent flow features are suppressed by turbulent diffusion. Specifically, in the upper region of the inner liner, the SBES solution (b_1) predicts the formation of a more effective cooling film layer along the wall, resulting in lower metal temperatures compared to the RANS case (a_1). In the slot region of the outer liner, SBES (b_2) shows a more pronounced jet separation and recirculation, as visible in the mixing field. However, this behaviour has a negligible effect on wall temperatures, likely because the recirculating flow interacts weakly with the surface cooling mechanisms.

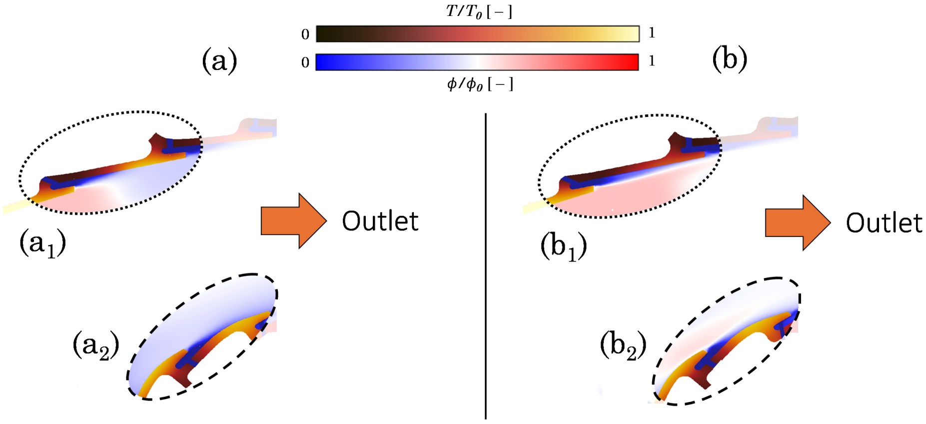

Figure 11. Comparison of mixing field and liner metal temperature in the nugget region between RANS (**a**) and SBES (**b**) simulations under TP A operating conditions.

These findings underscore the robustness of the correlation-based methodology when coupled with CFD and support its application in early design stages of combustor cooling systems, where full conjugate heat transfer (CHT) simulations may be prohibitively expensive.

To further improve agreement with experimental data, a second numerical campaign was carried out using the TP A model, with the aim of identifying correction factors for the HTC values used in the one-dimensional model. This tuning step was necessary due to the high sensitivity of empirical correlations to local fluid-dynamic parameters, particularly in geometrically complex regions like the nuggets. While in the ribbed region the flow is well-guided, allowing for accurate Reynolds number estimation, in the nugget region, flow passage areas vary significantly, making the definition of reference parameters for correlation input ambiguous and error-prone.

To mitigate this, corrective coefficients were introduced for the HTC on the outer walls of the liners. These coefficients were calibrated based on the thermocouple measurements and are summarised in Table 1. It should be noted that the reported values of the tuning coefficients have been uniformly scaled due to confidentiality constraints, and should therefore be interpreted in a relative rather than an absolute sense. As expected, the tuning factors for the nugget region are notably higher than those for the ribbed section, underlining the critical role of accurate fluid-dynamic parameter estimation for reliable application of empirical correlations. Interestingly, the corrective coefficients for the inner liner in the nugget region show contrasting trends between the RANS and SBES simulations. This confirms that the choice of turbulence-modelling approach significantly affects the jet–flow interaction and heat transfer prediction, and that the SBES solution cannot be simply tuned based on results from a RANS simulation.

Table 1. Scaled tuning coefficients for the HTC computation.

	Ribbed Duct HTC_{tuned}/HTC_{corr}	**Nugget I** HTC_{tuned}/HTC_{corr}	**Nuggets II–III** HTC_{tuned}/HTC_{corr}
SBES Inner Liner	5.5	3.5	3.0
RANS Inner Liner	5.5	9.5	17.0
SBES Outer Liner	4.5	2.0	7.0
RANS Outer Liner	4.5	3.5	7.5

The impact of these tuning coefficients is illustrated in Figures 12 and 13, showing both qualitative and quantitative improvements in predicted wall temperatures along the cold side of the liners. The results confirm that after tuning, both RANS and SBES simulations accurately reproduce the experimental temperature profiles. However, the magnitude of the applied HTC corrections, particularly in the nugget region, highlights the inherent overprediction of thermal loads by RANS due to its inability to capture the unsteady and three-dimensional mixing processes. This reinforces the importance of adopting scale-resolving approaches such as SBES when accurate thermal load prediction is required in complex flow environments.

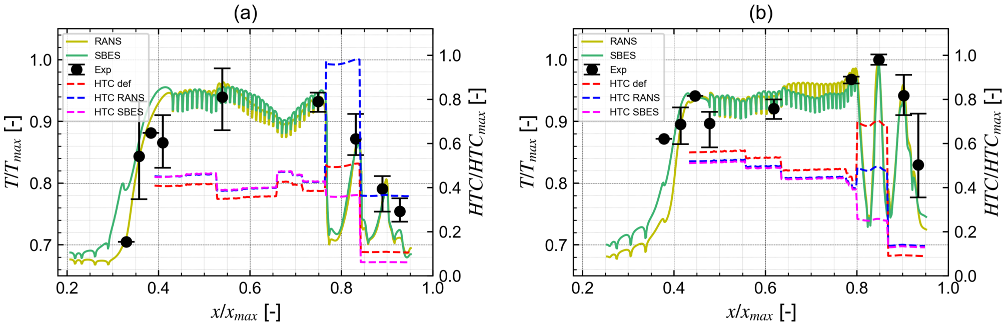

Figure 12. Normalised wall temperature and HTC distribution along the centerline of the cold-side walls for the inner liner (**a**) and outer liner (**b**) following the tuning of the HTC correction factors within the 1D model.

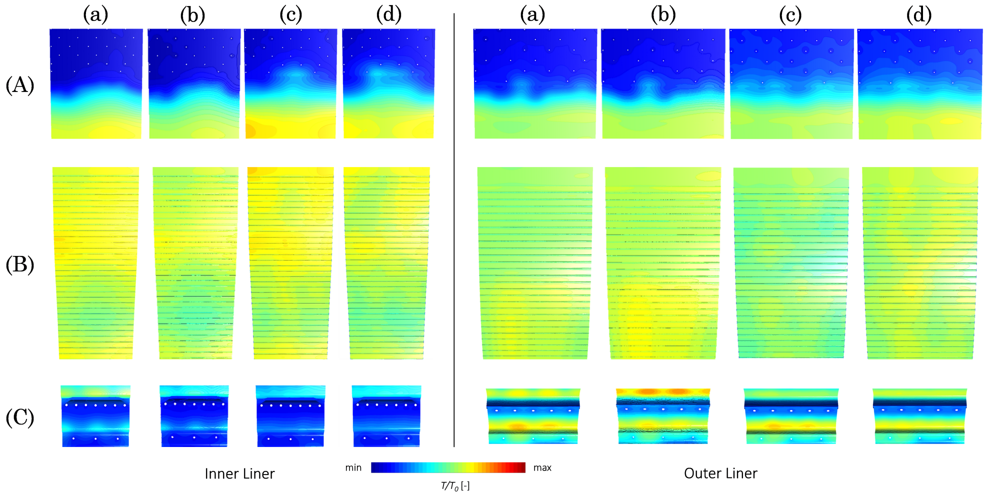

Figure 13. Comparison of wall temperature distribution on the cold side of the liner between RANS and SBES simulations, before and after tuning the HTC correction factors in the 1D model. (**a**) RANS without HTC correction; (**b**) RANS with HTC correction; (**c**) SBES without HTC correction; (**d**) SBES with HTC correction. Zones A, B, and C correspond to the three main liner sections, as indicated in Figure 1b.

5.1.3. Heat Shield Wall Temperature Distributions

The analysis of heat shield wall temperature is critical for optimising thermal management in combustors. While the previous section focused on predicting liner wall temperatures using a one-dimensional correlation-based model to estimate the external HTC, thus avoiding the need to mesh and solve the full cooling flow domain, the heat shield presents a different scenario. Fully immersed within the combustion chamber and surrounded by a resolved flow, it does not require a dedicated thermal load model. Consequently, this analysis is limited to a comparison between the RANS and SBES approaches. The goal is to highlight the impact of the turbulence-modelling strategy on thermal load prediction, offering insights into the most effective approach during the preliminary design phase.

It is important to note that to ensure compatibility with the periodic boundary conditions in the computational domain, the distribution of impingement jet holes was slightly adjusted to avoid truncated holes at the periodic interfaces, while preserving the same global cooling mass flow rate as in the test article. Although experimental thermocouple measurements are reported for reference, these geometric differences limit the validity of a direct, quantitative comparison. Therefore, the focus of this analysis should not be on determining which modelling approach is "more accurate" against experimental data, but rather on assessing the relative differences in flow and thermal predictions between the RANS and SBES methodologies.

The predicted temperature distributions on the heat shield are shown in Figure 14, which provides a qualitative comparison between RANS and SBES results. These contours highlight the impact of the turbulence-modelling approach on the thermal field and its interaction with the cooling flow. In particular, the SBES simulation reveals consistently higher temperatures near the component ends, which can be attributed to the partial recirculation of hot combustion gases into the impingement exhaust gap, a feature more prominently captured by SBES due to its improved resolution of turbulent structures and jet interactions (see also Figure 15). This limited backflow of hot gas is absent in the RANS simulation, indicating a less diffused interaction between the core flow and the cooling jets.

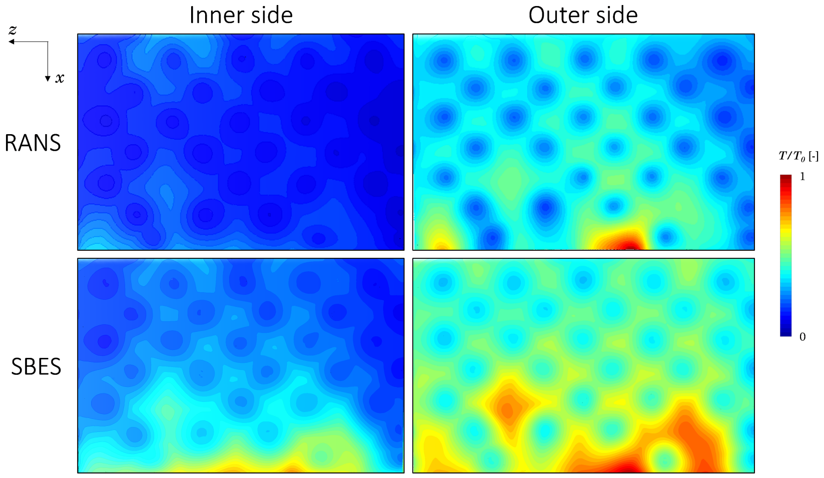

Figure 14. Comparison of wall temperature distribution on the cold side of the heat shield between RANS and SBES simulations under the TP A operating conditions.

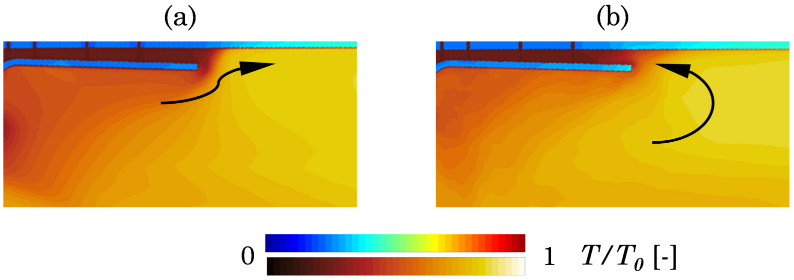

Figure 15. Temperature field around the heat shield under TP A operating conditions: comparison between RANS (**a**) and SBES (**b**) simulations. The SBES results clearly reveal an intermittent reverse flow of hot gases at the ends of the heat shield, leading to increased thermal loading and higher average wall temperatures compared to RANS. Distinct colourmaps are applied to the solid and fluid domains to improve clarity.

A more quantitative assessment is provided in Figure 16, which compares one-dimensional wall temperature profiles along the curvilinear axis of the heat shield's symmetry plane for both RANS and SBES simulations against experimental thermocouple data. The SBES simulation predicts higher temperatures in the downstream region, consistent with the hot gas residual backflow previously discussed. However, the absolute overprediction relative to experimental measurements, particularly on the inner liner side, can be attributed not only to the flow physics but also to slight differences in the geometry between the experimental hardware and the simulated domain. As mentioned earlier, the impingement hole distribution was modified in the CFD model to enable periodic boundary conditions, deviating from the actual hardware configuration. As a result, a strict pointwise comparison with experimental data is not feasible in this portion of the domain. Instead, the focus should be placed on the relative performance of RANS and SBES in capturing the aerothermal behaviour, rather than on determining which approach best matches the experimental measurements.

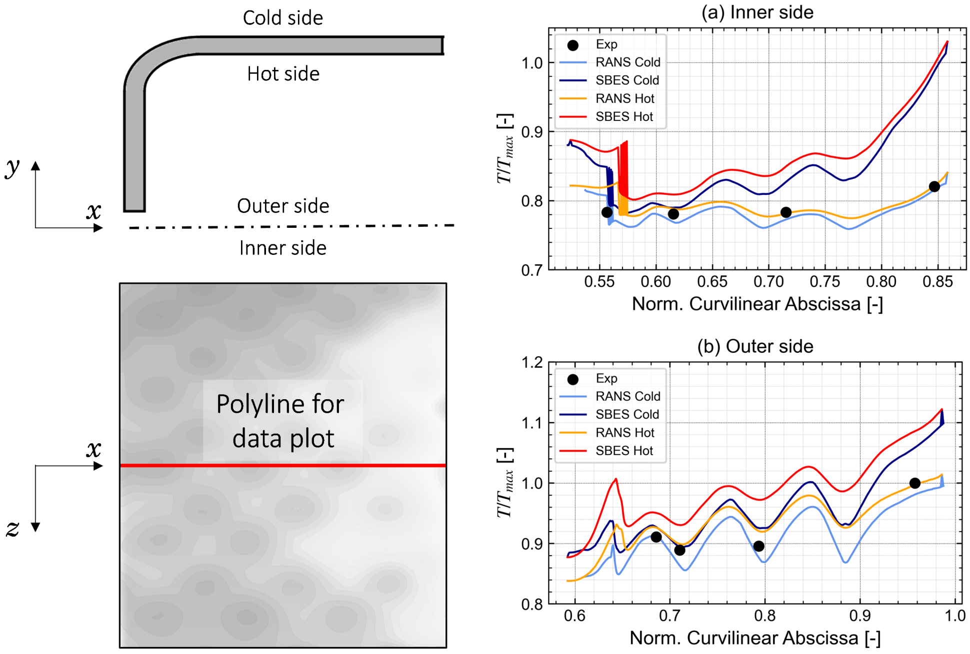

Figure 16. Comparison of wall temperature distribution along the centerline of both the cold and hot sides of the heat shield between RANS and SBES simulations under TP A operating conditions.

5.2. Test Point B

The objective of analysing a second operating point is to evaluate whether the numerical model, originally fine-tuned for the previous condition (TP A), can reliably predict cold-side thermal loads for different operating conditions using only updated boundary conditions. In essence, the study investigates whether the correction factors defined for one specific test point are transferable or if a dedicated tuning process is necessary for each operating point to ensure accurate predictions with the one-dimensional correlation-based model. To perform this assessment, the calibrated model from TP A is applied directly to a new test point, TP B. This operating point is characterised by an overall lower thermal load and a significantly unbalanced fuel distribution across the combustor burners. As a result, strong thermal gradients arise within the combustion chamber, causing markedly different thermal loads on the inner and outer liners. Both RANS and SBES simulations are carried out for this configuration.

5.2.1. Aerothermal Fields

In line with the previous analysis, a key characteristic of the TP B operating condition is the significantly uneven fuel distribution among the burners, with a larger fraction of the total fuel mass flow directed toward the outer injectors (see Figure 17). This imbalance strongly influences the combustor's thermal field, creating pronounced asymmetries in heat release and thermal loading between the two liners.

Figure 18 illustrates the instantaneous and time-averaged distributions of normalised temperature and axial velocity along the longitudinal burner plane for TP B, as predicted by both RANS and SBES approaches. Compared to TP A, TP B exhibits a localised high-temperature region concentrated near the outer liner, directly resulting from the skewed fuel injection.

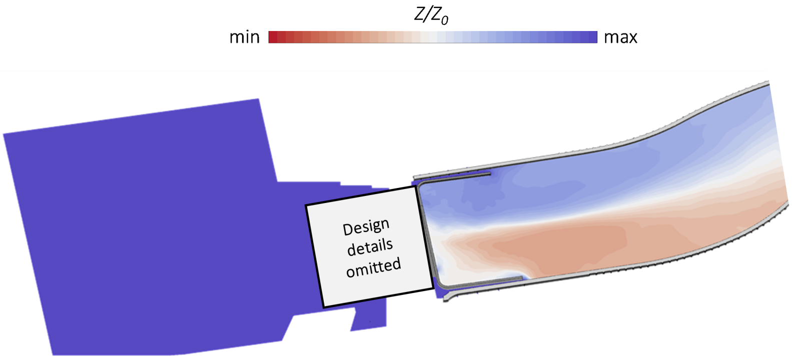

Figure 17. Normalised time-averaged mixture fraction field on a longitudinal midplane of the burner from the TP B SBES simulation. The solid domain is included to better illustrate the interaction between cooling flows and the combustor walls.

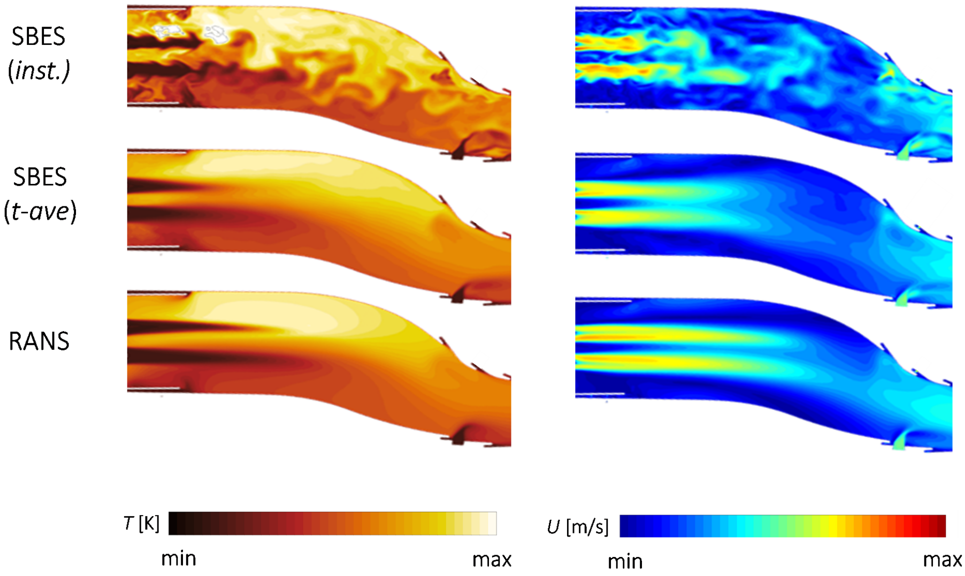

Figure 18. Normalised temperature and axial velocity fields on a longitudinal plane of the burner from TP B RANS and SBES simulations. The SBES results include both instantaneous and time-averaged data.

Despite these variations in fuel distribution and overall thermal input, the global aerodynamic structure of the flow remains broadly consistent with TP A. However, the non-uniform heat release leads to a markedly asymmetric temperature field within the combustion chamber. As a result, thermal loading on the outer liner remains comparable to

TP A, while the inner liner experiences a significantly reduced thermal load. This disparity leads to substantial differences in predicted wall temperatures between the two liners.

More importantly, such extreme thermal asymmetry poses a critical test for the robustness of the correlation-based model previously tuned for TP A. Since TP B represents the most thermally unbalanced and operationally distinct case from TP A, it challenges the validity of directly applying the same correction factors without further adjustments. The model's ability to maintain predictive accuracy under these conditions is therefore a strong indicator of its generalisability and reliability.

5.2.2. Liner Wall Temperature Distributions

As previously highlighted, simulations on the new test point utilised a fine-tuned 1D model, calibrated with parameters from the TP A investigation (detailed in Table 1). This setup enables evaluation of the model's robustness when applied to significantly different combustion scenarios, without re-tuning. The first result, presented in Figure 19, compares the cold-side wall temperature distributions between TP A and TP B using the SBES approach. As expected, the overall thermal loading on the combustor is lower under TP B conditions, with minimal heat transfer on the inner liner, consistent with the skewed combustion distribution toward the outer liner observed in Figure 18.

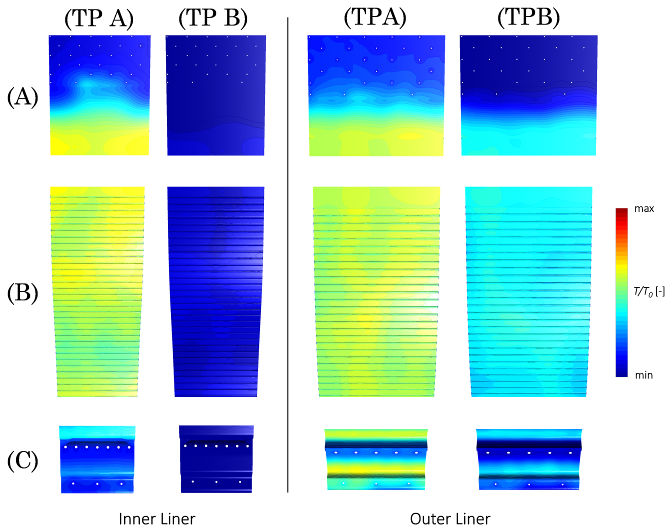

Figure 19. Comparison of wall temperature distribution on liners' cold side between TP A and TP B utilising an SBES approach: (**A**) perforated plain duct, (**B**) ribbed duct, (**C**) nugget region.

Further insight is provided in Figure 20, which compares the thermal powers absorbed by the liners under the two operating conditions. These results demonstrate the model's ability to accurately capture the redistribution of thermal loads across the combustor, reinforcing its utility in predicting component-level thermal behaviour across different regimes.

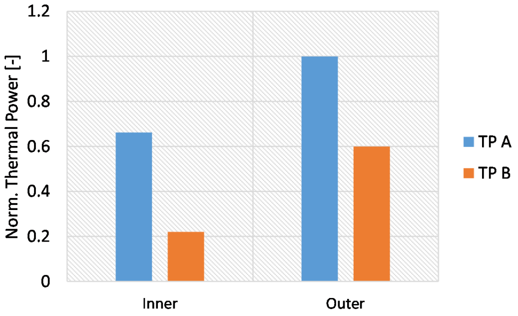

Figure 20. Comparison of thermal powers between the two analysed operational conditions.

Figure 21 displays the normalised wall temperature and heat transfer coefficient profiles along the cold-side centerlines of both liners, including results from both RANS and SBES simulations, compared to thermocouple measurements. For this test point, the model maintains good predictive accuracy, particularly on the outer liner, which bears the majority of the thermal load. The underestimation observed in the ribbed region of the outer liner may be attributed to the use of correction factors derived from TP A, which reduce the HTC under lower coolant mass flow rates. This, in turn, leads to reduced convective absorption and lower coolant temperatures, slightly lowering predicted metal temperatures—an effect more evident in the RANS solution.

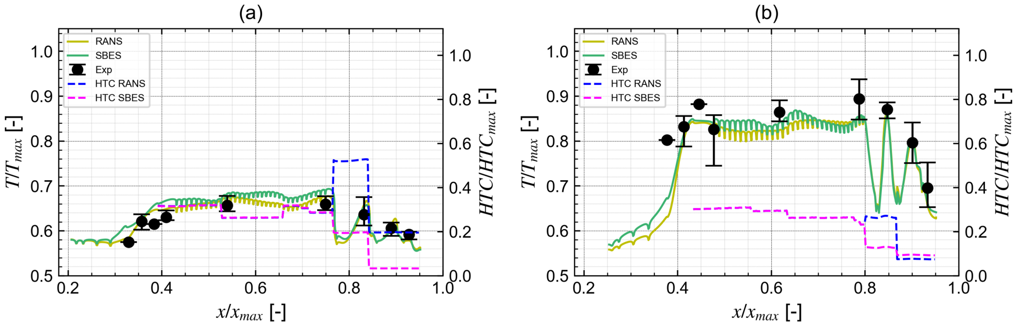

Figure 21. Normalised wall temperature and HTC distribution along the centerline of the cold-side walls for the inner liner (**a**) and outer liner (**b**) following the tuning of the HTC correction factors within the 1D model performed on TP A.

Despite these local discrepancies, the one-dimensional correlation-based model maintains robust predictive accuracy, with relative differences from experimental measurements staying within the typical bounds of engineering tolerances. This confirms the model's capacity to extend beyond its initial calibration point and reliably predict wall temperatures under varying boundary conditions.

Turning to the RANS vs. SBES comparison, the trends observed for TP A are largely confirmed for TP B. SBES again shows enhanced ability to resolve turbulence-driven flow structures, leading to more physically realistic heat transfer coefficients, particularly in critical areas such as the nugget region. Here, SBES provides more reliable HTC values for a given wall temperature, whereas RANS continues to exhibit greater sensitivity and uncertainty, reinforcing the difficulty of determining accurate HTC values a priori with a steady approach.

5.2.3. Heat Shield Wall Temperature Distributions

For the metal temperatures on the heat shield surfaces depicted in Figures 22 and 23, a notable trend persists in the SBES simulations of this second operating cycle, showing an increasing temperature gradient towards the heat shield's trailing edge near the outer liner. This is likely due to a localised residual backflow of hot gases into the gap. Conversely, the RANS simulations exhibit a decreasing temperature gradient in the same region, likely because of a more consistent flow exiting the gap and reduced thermal load on the inner liner. This limits heat removal by the impinging air, resulting in lower temperatures near the gap exit. Overall, the results for this operating condition show improvements over those observed for TP A.

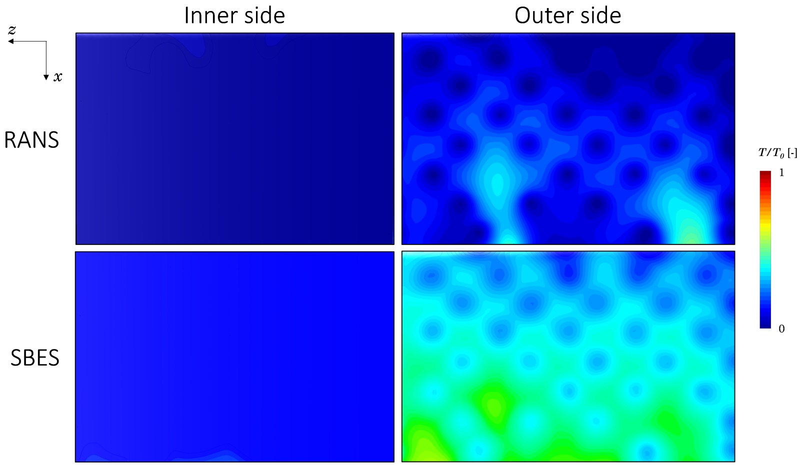

Figure 22. Comparison of wall temperature distribution on the cold side of the heat shield between RANS and SBES simulations under the TP B operating conditions.

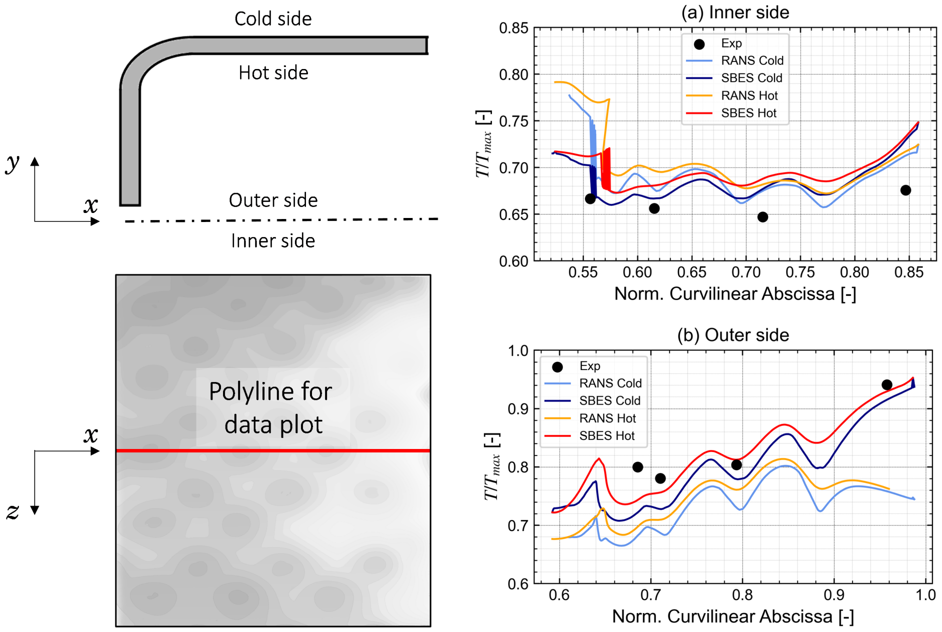

Figure 23. Comparison of wall temperature distribution along the centerline of both the cold and hot sides of the heat shield between RANS and SBES simulations under TP B operating conditions.

Consistent with the findings for TP A, the results obtained with the two fine-tuned numerical approaches are nearly identical on the outer liner. However, significant thermal differences are observed on the inner liner, likely due to the increased turbulent mixing in the SBES simulation, which leads to greater transport of hot gases near the inner liner compared to the RANS simulation.

However, despite using the numerical procedure specifically tuned with TP A parameters, the agreement between the numerically predicted temperatures and experimental data is good, with maximum differences on the order of 40 K at the very end of the outer liner ribbed duct.

6. Computational Costs

All numerical simulations presented in this study were carried out on a high-performance computing (HPC) cluster composed of 20 nodes, each equipped with multi-core Intel® Xeon® Gold 6248 processors. The scale-resolving SBES simulations, including the transient averaging phase required to extract statistically meaningful flow and thermal fields, demanded a total computational effort of approximately 50,000 CPU hours. In stark contrast, the steady-state RANS simulations achieved convergence with only around 10,000 CPU hours, underlining the substantial disparity in computational expense between unsteady and steady modelling strategies.

This difference becomes particularly relevant when considering more comprehensive configurations that also include the cold-side cooling flow domain, such as the ribbed annular ducts and the plenum region above the nuggets, within a loosely coupled CHT framework. Adding these internal fluid regions would introduce an estimated 10–15 million additional polyhedral cells and at least one more fluid-solid interface requiring coupling. Even under a loosely coupled scheme, this would significantly increase computational demands, particularly in SBES, where accurate resolution of turbulent structures in the internal cooling passages would require finer meshes and smaller time-steps. In this scenario, the total cost of an SBES-based loosely coupled CHT simulation is estimated to easily exceed 100,000 CPU hours. The RANS-based counterpart, although more affordable, would still incur notable increases in runtime and memory usage. These considerations reinforce the advantage of the proposed hybrid, multi-fidelity methodology, relying on RANS/SBES simulations of the hot gas path coupled with a 1D correlation-based thermal load model for the cold side, which offers a practical and efficient balance between fidelity and cost. This makes it especially suitable for preliminary design phases and parametric studies across multiple operating points.

7. Conclusions

In this work, numerical conjugate heat transfer analyses were conducted to determine the metal temperatures of the NovaLT™16 combustor liners. The objective was to validate a 1D correlational model for predicting cold-side thermal loads on the liners. A RANS and SBES campaign was conducted for the TP A operating condition to calibrate the 1D model and adapt the one-dimensional correlational approach to the real 3D problem. Subsequently, the calibrated 1D model was tested and validated through RANS and SBES simulations for a different combustor operating condition (TP B), characterised by lower thermal loads and a different fuel distribution through the injection system.

The results of the present activity show that, by appropriately defining the zones for applying various correlations to different liner portions, the proposed numerical solution is robust. The coupled model with CFD simulations accurately predicts the cold-side thermal loads on the liners for both RANS and SBES approaches, even without tuning, suggesting the possibility of its use during the initial stages of the cooling system design, with significantly reduced computational cost compared to simulating the entire system. The flexibility of this defined tool is confirmed by good agreement with experimental results for varying operating conditions.

The primary challenges of the model are observed near the nugget regions, where uncertainties arise, including the a priori definition of fluid-dynamic quantities for correlation use. These uncertainties are influenced by the specific flow passages considered, necessitating further detailed study to define them accurately and establish a standardised procedure for their application.

In general terms, the 1D correlation-based model performs best when the cooling sector geometries closely match the categories for which the correlations were developed. Its accuracy increases when the flow exhibits predominantly two-dimensional behaviour. Conversely, applying the model to highly custom geometries or strongly three-dimensional flows is more challenging, as exemplified by the uncertainties observed in the nugget regions. Nevertheless, it is important to emphasise that this tool is primarily intended for the design phase, where geometries are still in a building stage and detailed 3D resolution is not yet required.

Regarding turbulence modelling, the RANS and SBES approaches exhibited broadly similar performance across much of the domain, with meaningful differences emerging in highly three-dimensional flow regions. In particular, within the nugget region, the SBES approach provided more realistic heat transfer coefficient values for a given wall temperature. This suggests that RANS may overestimate thermal loads in such complex regions, making its HTC predictions more difficult to determine a priori.

Significant differences also appeared in the heat shield wall temperature distribution. While RANS predictions showed closer agreement with experimental measurements in certain regions, this cannot be interpreted as evidence of superior modelling accuracy. As previously discussed, small geometric discrepancies, specifically in the impingement hole layout introduced to enforce periodicity in the CFD model, limit the validity of direct comparisons with experimental data. These findings underscore that the differences between RANS and SBES are driven by how each approach captures flow physics, particularly hot gas unsteadiness, backflow, and jet interaction, rather than simple numerical accuracy.

Given its lower computational cost, RANS coupled with the 1D correlation-based model remains a practical and valuable tool for early-stage design analysis, offering reasonable wall temperature predictions across multiple operating conditions. However, care must be taken when applying RANS to regions dominated by strong three-dimensional flow features, where the improved physical fidelity of SBES may be necessary to avoid misleading thermal predictions.

Author Contributions: Conceptualization, G.R., and A.A.; methodology, G.R., and A.A.; validation, G.L., S.G., and G.R.; formal analysis, G.L.; investigation, G.L.; resources, S.G., and G.R.; data curation, G.L., and S.G.; writing—original draft preparation, G.L.; writing—review and editing, G.L., S.G., G.R., and A.A.; visualization, G.L., and S.G.; supervision, S.G., G.R., and A.A.; project administration, A.A.; funding acquisition, A.A. All authors have read and agreed to the published version of the manuscript.

Funding: This research was funded by Baker Hughes.

Data Availability Statement: The data used in this study were obtained from Baker Hughes and are not publicly available due to confidentiality agreements.

Acknowledgments: The authors gratefully acknowledge the financial support provided by Baker Hughes. They also wish to thank Dott. Ing. Simone Paccati and Dott. Ing. Alberto Amerini for their valuable contributions to the development of the tool and the numerical setup strategy.

Conflicts of Interest: Authors Stefano Gori and Giovanni Riccio were employed by the company Baker Hughes. The remaining authors declare that the research was conducted in the absence of any commercial or financial relationships that could be construed as a potential conflict of interest.

Abbreviations

The following abbreviations are used in this manuscript:

Acronyms	
CFD	Computational Fluid Dynamics
CHT	Conjugate Heat Transfer
FGM	Flamelet Generated Manifold
FTT	Flow-Through-Time
GR	Growth Rate
GRI	Gas Research Institute
HS	Heat Shield

HTC	Heat Transfer Coefficient
LES	Large Eddy Simulation
PDF	Probability Density Function
PI	Pope Index
RANS	Reynolds-Averaged Navier–Stokes
RMSE	Root Mean Squared Error
SBES	Stress-Blended Eddy Simulation
SDES	Shielded Detached Eddy Simulation
SIMPLEC	Semi-Implicit Method for Pressure Linked Equations-Consistent
STS	Solid Time-Step
TBC	Thermal Barrier Coating
TFSC	Turbulent Flame Speed Closure
TP	Test Point
Symbols	
A	Zimont TFSC model constant
b	Height of the duct [m]
c	FGM unnormalised reaction progress variable [-]
C_s	Smagorinsky constant [-]
D_H	Hydraulic diameter [m]
e	Height of the turbulator [m]
f_s	Shielding function [-]
k	Turbulent kinetic energy [m^2 s^{-2}]
l	Characteristic length [m]
l_t	Turbulent length scale [m]
Nu	Nusselt number [-]
p	Pitch of the turbulator [m]
Pr	Prandtl number [-]
Re	Reynolds number [-]
S	Laminar flame speed [m s^{-1}]
S	Turbulent flame speed [m s^{-1}]
u	Velocity [m s^{-1}]
T	Temperature [K]
w	Width of the turbulator [m]
Z	Mixture fraction [-]
Greek	
α	Thermal diffusivity of the unburnt gas [m^2 s^{-1}]
Δ	Cell characteristic length [m]
ϵ	Turbulent kinetic energy dissipation rate [m^2 s^{-3}]
θ	Rib angle [rad]
λ	Thermal conductivity [W m^{-1} K^{-1}]
ν_t	Eddy viscosity [m^2 s^{-1}]
ρ	Density [kg m^{-3}]
τ_{ij}	Modelled stress sensor
ϕ	Generic thermodynamic state
ω	Specific turbulent kinetic energy dissipation rate [s^{-1}]
$\dot{\omega}_c$	Turbulent progress variable source term [1/s]
Subscripts	
free	Freestream quantity
RANS	RANS modelled quantity
res	Resolved quantity
SBES	SBES modelled quantity
sgs	Sub-grid scale modelled quantity
u	Unburnt gas quantity
Superscripts	

$\sim$	Favre averaged
$'$	Reynolds fluctuation
$''2$	Variance

References

1. Moon, H.; Kim, K.M.; Jeon, Y.H.; Shin, S.; Park, J.S.; Cho, H.H. Effect of thermal stress on creep lifetime for a gas turbine combustion liner. *Eng. Fail. Anal.* **2015**, *47*, 34–40. [CrossRef]
2. Wurm, B.; Schulz, A.; Bauer, H.J.; Gerendas, M. Cooling Efficiency for Assessing the Cooling Performance of an Effusion Cooled Combustor Liner. In Proceedings of the ASME Turbo Expo 2013: Turbine Technical Conference and Exposition, San Antonio, TX, USA, 3–7 June 2013; Volume 3B: Heat Transfer, p. V03BT13A010. [CrossRef]
3. Yin, F.; Rao, A.G. A review of gas turbine engine with inter-stage turbine burner. *Prog. Aerosp. Sci.* **2020**, *121*, 100695. [CrossRef]
4. Yin, F.; Gangoli Rao, A. Performance analysis of an aero engine with inter-stage turbine burner. *Aeronaut. J.* **2017**, *121*, 1605–1626. [CrossRef]
5. Andrews, G.E.; Asere, A.A.; Gupta, M.L.; Mkpadi, M.C. Full Coverage Discrete Hole Film Cooling: The Influence of Hole Size. In Proceedings of the ASME 1985 International Gas Turbine Conference and Exhibit, Houston, TX, USA, 18–21 March 1985; Volume 3: Heat Transfer; Electric Power, *Turbo Expo*, p. V003T09A003. [CrossRef]
6. Andrei, L.; Andreini, A.; Bianchini, C.; Caciolli, G.; Facchini, B.; Mazzei, L.; Picchi, A.; Turrini, F. Effusion Cooling Plates for Combustor Liners: Experimental and Numerical Investigations on the Effect of Density Ratio. *Energy Procedia* **2014**, *45*, 1402–1411. [CrossRef]
7. Andreini, A.; Facchini, B.; Picchi, A.; Tarchi, L.; Turrini, F. Experimental and Theoretical Investigation of Thermal Effectiveness in Multiperforated Plates for Combustor Liner Effusion Cooling. *J. Turbomach.* **2014**, *136*, 091003. [CrossRef]
8. Boudier, G.; Gicquel, L.; Poinsot, T. Effects of mesh resolution on large eddy simulation of reacting flows in complex geometry combustors. *Combust. Flame* **2008**, *155*, 196–214. [CrossRef]
9. Murthy, J.Y.; Mathur, S.R. Computational Heat Transfer in Complex Systems: A Review of Needs and Opportunities. *J. Heat Transf.* **2012**, *134*, 031016. [CrossRef]
10. Rodriguez, J.; Cavadini, P.; Brunelli, M.; Custer, C.; Carpenter, C. High Fidelity CHT CFD for Gas Turbine Heat Transfer Application. In Proceedings of the 1st Global Power and Propulsion Forum, Zurich, Switzerland, 16–18 January 2014; Paper No. GPPF-2017-171.
11. Zhong, S.; Meng, F.; Zhang, H.; Gong, C.; Yan, B.; Yang, X.; Pan, K.; Chen, S. Effects of wall heat loss on the flame shape and preheat layer dynamics in a premixed swirling flame under varying turbulence intensities. *Energy* **2025**, *329*, 136447. [CrossRef]
12. Bioche, K.; Vervisch, L.; Ribert, G. Premixed flame-wall interaction in a narrow channel: Impact of wall thermal conductivity and heat losses. *J. Fluid Mech.* **2018**, *856*, 5–35. [CrossRef]
13. He, L. *Chapter Two—Conjugate Heat Transfer: Some Fundamentals and rEcent Progress*; Elsevier: Amsterdam, The Netherlands, 2023; Volume 55, pp. 41–87. [CrossRef]
14. Zhang, S.; Chen, F.; Liu, H. Time-Adaptive, Loosely Coupled Strategy for Conjugate Heat Transfer Problems in Hypersonic Flows. *J. Thermophys. Heat Transf.* **2014**, *28*, 635–646. [CrossRef]
15. He, L.; Fadl, M. Multi-scale time integration for transient conjugate heat transfer. *Int. J. Numer. Methods Fluids* **2017**, *83*, 887–904. [CrossRef]
16. Koren, C.; Vicquelin, R.; Gicquel, O. Self-adaptive coupling frequency for unsteady coupled conjugate heat transfer simulations. *Int. J. Therm. Sci.* **2017**, *118*, 340–354. [CrossRef]
17. Paccati, S.; Bertini, D.; Mazzei, L.; Andreini, A. Large-Eddy Simulation of a Model Aero-Engine Sooting Flame with a Multiphysics Approach. *Flow Turbul. Combust.* **2021**, *106*, 1329–1354. [CrossRef]
18. Andreini, A.; Da Soghe, R.; Facchini, B.; Mazzei, L.; Colantuoni, S.; Turrini, F. Local Source Based CFD Modeling of Effusion Cooling Holes: Validation and Application to an Actual Combustor Test Case. *J. Eng. Gas Turbines Power* **2013**, *136*, 011506. [CrossRef]
19. Gorman, J.M.; Sparrow, E.M.; Abraham, J.P.; Minkowycz, W.J.M. Evaluation of the efficacy of turbulence models for swirling flows and the effect of turbulence intensity on heat transfer. *Numer. Heat Transf. Part B Fundam.* **2016**, *70*, 485–502. [CrossRef]
20. Spalart, P. Detached-Eddy Simulation. *Annu. Rev. Fluid Mech.* **2009**, *41*, 181–202. [CrossRef]
21. Menter, F. Stress-Blended Eddy Simulation (SBES)—A New Paradigm in Hybrid RANS-LES Modeling. In *Notes on Numerical Fluid Mechanics and Multidisciplinary Design*; Springer: Cham, Switherland, 2018; Volume 137, pp. 27–37. [CrossRef]
22. Mira, D.; Perez-Sanchez, E.J.; Borrell, R.; Houzeaux, G. HPC-enabling technologies for high-fidelity combustion simulations. *Proc. Combust. Inst.* **2023**, *39*, 5091–5125. [CrossRef]
23. ANSYS. ANSYS Fluent Theory Guide. Southpointe 2600 Ansys Drive Canonsburg, PA 15317. 2022. Available online: http://www.ansys.com (accessed on 12 July 2025).

24. Amerini, A.; Paccati, S.; Andreini, A. Computational Optimization of a Loosely-Coupled Strategy for Scale-Resolving CHT CFD Simulation of Gas Turbine Combustors. *Energies* **2023**, *16*, 1664. [CrossRef]
25. Launder, B.; Sharma, B. Application of the energy-dissipation model of flow near a spinning disc. *Lett. Heat Mass Transfer* **1974**, 131–138. [CrossRef]
26. Kader, B. Temperature and concentration profiles in fully turbulent boundary layers. *Int. J. Heat Mass Transf.* **1981**, *24*, 1541–1544. [CrossRef]
27. Menter, F. Two-Equation Eddy-Viscosity Transport Turbulence Model for Engineering Applications. *AIAA J.* **1994**, *32*, 1598–1605. [CrossRef]
28. Lilly, D.K. A proposed modification of the Germano subgrid-scale closure method. *Phys. Fluids A Fluid Dyn.* **1992**, *4*, 633–635. [CrossRef]
29. Darwish, M.; Moukalled, F. A Fully Coupled Navier-Stokes Solver for Fluid Flow at All Speeds. *Numer. Heat Transf. Fundam.* **2014**, *65*, 410–444. [CrossRef]
30. Doormaal, J.P.V.; Raithby, G.D. Enhancements of the simple method for predicting incompressible fluid flows. *Numer. Heat Transf. Part A-Appl.* **1984**, *7*, 147–163. [CrossRef]
31. van Oijen, J.; Goey, P. Modelling of Premixed Laminar Flames using Flamelet-Generated Manifolds. *Combust. Sci. Technol.* **2000**, *161*, 113–137. [CrossRef]
32. Peters, N. Laminar flamelet concepts in turbulent combustion. In *Symposium (International) on Combustion*; Elsevier: Amsterdam, The Netherlands; 1988; Volume 21, pp. 1231–1250. [CrossRef]
33. Bilger, R. Reaction rates in diffusion flames. *Combust. Flame* **1977**, *30*, 277–284. [CrossRef]
34. Frenklach, M.; Wang, H.; Goldenberg, M.; Smith, G.; Golden, D.; Bowman, C.; Hanson, R.; Gardiner, W.; Lissianski, V. *GRI-Mech—An Optimized Detailed Chemical Reaction Mechanism for Methane Combustion*; Technical Report; Gas Research Institute Chicago: Des Plaines, IL, USA, 1995.
35. Zimont, V.; Polifke, W.; Bettelini, M.; Weisenstein, W. An Efficient Computational Model for Premixed Turbulent Combustion at High Reynolds Numbers Based on a Turbulent Flame Speed Closure. *J. Eng. Gas Turbines Power* **1998**, *120*, 526–532. [CrossRef]
36. Flohr, P.D.I.; Pitsch, H. A turbulent flame speed closure model for LES of industrial burner flows. *Proceedings of the Summer Program 2000*. 2001. Available online: https://web.stanford.edu/group/ctr/ctrsp00/flohr.pdf (accessed on 1 September 2025).
37. Han, J.; Glicksman, L.; Rohsenow, W. An investigation of heat transfer and friction for rib-roughened surfaces. *Int. J. Heat Mass Transf.* **1978**, *21*, 1143–1156. [CrossRef]
38. Han, J.C.; Park, J.S.; Lei, C.K. Heat Transfer Enhancement in Channels with Turbulence Promoters. *J. Eng. Gas Turbines Power* **1985**, *107*, 628–635. [CrossRef]
39. Han, J.; Park, J. Developing heat transfer in rectangular channels with rib turbulators. *Int. J. Heat Mass Transf.* **1988**, *31*, 183–195. [CrossRef]
40. Alkhamis, N.; Rallabandi, A.; Han, J.C. Heat Transfer and Pressure Drop Correlations for Square Channels with V-Shaped Ribs at High Reynolds Numbers. *J. Heat Transf.* **2011**, *133*, 111901. [CrossRef]
41. Wieghardt, K.; Tillmann, W. On the Turbulent Friction Layer for Rising Pressure. 1951. Available online: https://ntrs.nasa.gov/citations/19930093916 (accessed on 1 September 2025).